The Astrophysical Journal, 925:63 (13pp), 2022 January 20 https://doi.org/10.3847/1538-4357/ac313f

Extremely Broad Lyα Line Emission from the Molecular Intragroup Medium in Stephan's Quintet: Evidence for a Turbulent Cascade in a Highly Clumpy Multiphase Medium?

P. Guillard[1,2], P. N Appleton[3], F. Boulanger[4], J. M. Shull[5], M. D. Lehnert[1], G. Pineau des Forets[6,7], E. Falgarone[4], M. E. Cluver[8,9], C. K. Xu[10,11], S. C. Gallagher[12], and P. A. Duc[13]
[1] Sorbonne Université, CNRS, UMR 7095, Institut d'Astrophysique de Paris, 98bis bd Arago, F-75014 Paris, France
[2] Institut Universitaire de France, Ministère de l'Enseignement Supérieur et de la Recherche, 1 rue Descartes, 75231 Paris Cedex F-05, France
[3] Caltech/IPAC, MC 6-313, 1200 E. California Blvd., Pasadena, CA 91125, USA
[4] Laboratoire de Physique de l'Ecole Normale Supérieure, ENS, Université PSL, CNRS, Sorbonne Université, Université de Paris, F-75005 Paris, France
[5] CASA, Astrophysical and Planetary Sciences Dept., University of Colorado, UCB-389, Boulder, CO 80309, USA
[6] Observatoire de Paris, PSL University, Sorbonne Université, LERMA, F-75014 Paris, France
[7] Université Paris Saclay, CNRS, Institut d'Astrophysique Spatiale, F-91405 Orsay, France
[8] Centre for Astrophysics and Supercomputing, Swinburne University of Technology, John Street, Hawthorn 3122, Victoria, Australia
[9] Department of Physics and Astronomy, University of the Western Cape, Robert Sobukwe Road, Bellville, South Africa
[10] IPAC, Caltech, MC 100-22, 1200 E. California Blvd., Pasadena, CA 91125, USA
[11] Chinese Academy of Sciences South America Center for Astronomy, National Astronomical Observatories, CAS, Beijing 100101, People's Republic of China
[12] Department of Physics and Astronomy, University of Western Ontario, London, ON N6A 3K7, Canada
[13] Université de Strasbourg, CNRS, Observatoire astronomique de Strasbourg, UMR 7550, F-67000 Strasbourg, France
Received 2021 February 12; revised 2021 October 18; accepted 2021 October 18; published 2022 January 26

Abstract

We present Hubble Space Telescope Cosmic Origin Spectrograph (COS) UV line spectroscopy and integral-field unit (IFU) observations of the intragroup medium in Stephan's Quintet (SQ). SQ hosts a 30 kpc long shocked ridge triggered by a galaxy collision at a relative velocity of 1000 km s^{-1}, where large amounts of molecular gas coexist with a hot, X-ray-emitting, plasma. COS spectroscopy at five positions sampling the diverse environments of the SQ intragroup medium reveals very broad (≈2000 km s^{-1}) Lyα line emission with complex line shapes. The Lyα line profiles are similar to or much broader than those of Hβ, [C II]157.7 μm, and CO (1–0) emission. The extreme breadth of the Lyα emission, compared with Hβ, implies resonance scattering within the observed structure. Scattering indicates that the neutral gas of the intragroup medium is clumpy, with a significant surface covering factor. We observe significant variations in the Lyα/Hβ flux ratio between positions and velocity components. From the mean line ratio averaged over positions and velocities, we estimate the effective escape fraction of Lyα photons to be ≈10%–30%. Remarkably, over more than four orders of magnitude in temperature, the powers radiated by X-rays, Lyα, H_2, and [C II] are comparable within a factor of a few, assuming that the ratio of the Lyα to H_2 fluxes over the whole shocked intragroup medium stay in line with those observed at those five positions. Both shocks and mixing layers could contribute to the energy dissipation associated with a turbulent energy cascade. Our results may be relevant for the cooling of gas at high redshifts, where the metal content is lower than in this local system, and a high amplitude of turbulence is more common.

Unified Astronomy Thesaurus concepts: Galaxy groups (597); Hickson compact group (729); Galaxy mergers (608); Galaxy interactions (600); Interacting galaxies (802); Intergalactic medium phases (814); Intergalactic medium (813); Cool intergalactic medium (303); Galaxy evolution (594); Galaxy processes (614); Galaxy quenching (2040); Interstellar dust (836)

Supporting material: machine-readable tables

1. Introduction

Galaxy interactions are important phases of galaxies' evolution, often involving high-speed shocks and dissipation or large amounts of kinetic energy. Many of these interactions are observed in infrared (IR) and visible light to trigger bursts of star formation. The dissipation of kinetic energy affects the gas cooling and how, when, and where star formation proceeds. To make headway in our understanding of the conversion of molecular gas to stars, it is crucial to determine the mechanism and rate of gas cooling.

Stephan's Quintet (HCG 92; hereafter SQ) is a compact group of five interacting galaxies (Arp 1973) with a complex dynamical history, involving multiple galaxy collisions (Moles et al. 1997; Renaud et al. 2010; Hwang et al. 2012; Duc et al. 2018). It is an ideal laboratory for the study of galaxy interactions and their impact on the physical state and energetics of the gas, especially the dissipation of merger-driven turbulence isolated against the dark sky (Guillard et al. 2009). It is one of the few extragalactic sources where one can spatially separate star-forming regions from shocked gas. When excluding the large foreground dwarf galaxy NGC 7320, the main group is dominated by four large massive galaxies. Three of them, NGC 7317, NGC 7318a, and NGC 7319, have heliocentric radial velocities in the range $V_{\rm helio} = 6599$–6747 km s^{-1}, and together they define the main barycentric velocity of the group (at around 6600 km s^{-1}). A fourth galaxy,

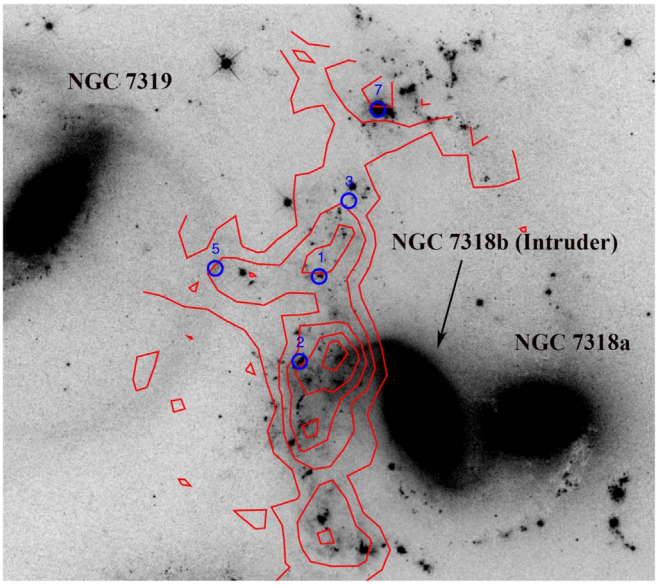

Figure 1. HST Wide Field Camera 3 F665N image of the inner SQ group with Spitzer IRS H_2 (0–0) S(3) 9.6 μm line flux contours in red from Cluver et al. (2010). This emission from warm molecular hydrogen highlights the North-South shocked ridge of the intragroup medium, as well as an extension toward NGC 7319, called "the bridge." The blue circles are the COS apertures (2.″5 in diameter) corresponding to 1.1 kpc at a distance $D = 94$ Mpc. The positions, observing parameters and integration times are listed in Table 1.

NGC 7318b ($V_{\rm helio} = 5774\,{\rm km\,s^{-1}}$, is often described as an intruder galaxy, because it appears to be colliding into NGC 7319's tidal tail in the intragroup medium at a relative velocity of $\approx$1000 km s^{-1} (see Figure 1 and Xu et al. 2003).

The collision of NGC 7318b with the gas in the intragroup medium is believed to be responsible for a striking feature of the group, namely a galaxy-wide shock ($\approx 15 \times 35\,{\rm kpc^2}$; Figure 1) seen at many wavelengths. A ridge of X-ray (O'Sullivan et al. 2009) and radio synchrotron (Allen & Hartsuiker 1972) emission from the hot (6×10^6 K) postshock plasma is associated with the group-wide shock. Surprisingly, Spitzer IRS spectroscopy revealed that the mid-IR spectrum in the intragroup medium is dominated by the rotational lines of H_2 (see red contours on Figure 1), with very weak dust emission from star formation (Appleton et al. 2006; Cluver et al. 2010). Over the shock region, no H I emission is detected, but optical line emission from ionized gas is observed at the velocity of NGC 7319's H I tidal tail (Sulentic et al. 2001).

The weakness of the mid-IR tracers of star formation (dust features and ionized gas lines) relative to the H_2 lines suggests that, despite the large H_2 mass estimated to be $\approx 5 \times 10^9\,M_\odot$(Guillard et al. 2012), the star formation rate is on average very low in the shock ($<0.07\,M_\odot$ yr^{-1}, Cluver et al. 2010). This is a factor 40 below the star formation rate expected from the Schmidt–Kennicutt relation (Guillard et al. 2012). Deep HST/WFC3 Hα imaging of SQ reveals many compact Hα knots and filaments spread over the shock, as well as a diffuse, underlying component (Gallagher et al. 2001). Extensive Gemini optical spectroscopy of 50 Hα knots in the group (Konstantopoulos et al. 2014) shows that both photoionization and shock excitation are present (see also Xu et al. 2003 for earlier long-slit optical spectroscopy), a result that is also confirmed by IFU spectroscopy (Duarte Puertas et al. 2019). Some knots are star clusters (masses from 10^4 to a few $10^5\,M_\odot$, Gallagher et al. 2001; Fedotov et al. 2011), while others show very strong [O III]λ 5007 Å and [O I]λ 6300 Å emission, and very broad (FWHM up to $\approx$700 km s^{-1}), complex optical emission line profiles, consistent with pure shock excitation (Konstantopoulos et al. 2014).

Spitzer and Herschel have shown that the H_2, [C II]λ158 μm and [O I]λ63 μm IR lines are important coolants of the shocked gas (Appleton et al. 2013, 2017). Guillard et al. (2009) proposed a model in which this line emission is powered by the dissipation of kinetic energy, through a turbulent cascade of energy, from the galaxy-wide shock down to low-velocity shocks within molecular gas. GALEX imaging of SQ (Xu et al. 2005) shows that most of the UV emission in the intragroup medium ridge is associated with an arc-like structure to the South-East of the intruder NGC 7318, which spatially correlates with a chain of Hα knots. The broadband UV emission at the center of the shock, where the H_2 emission peaks, is extended and corresponds to a radiation field of average intensity $G_{\rm UV} = 1.4$ Habing (Guillard et al. 2010).

This paper complements the rich array of SQ observations by presenting UV spectra obtained with HST COS, focusing on the Lyα line emission. We assess the origin of the Lyα photons and their contribution to the energy budget of the SQ galaxy collision. The comparison of the line profiles with those of CO, [C II] and Hβ provide insight on the structure of the multiphase ISM in SQ.

We assumed a distance to Stephan's Quintet of 94 Mpc for $H_0 = 70$ km s^{-1} Mpc^{-1}, and a group systemic heliocentric velocity of 6600 km s^{-1}.

2. Observations and Data Reduction

2.1. Observed COS Lines of Sight

We chose to perform deep COS spectroscopy of 5 regions in the intragroup medium of SQ, as shown on Figure 1 as detailed in Table 1, for which we have very high signal-to-noise ratio optical spectra from Gemini. The COS pointings are also associated with CO(1–0) line emission detected with the NOEMA interferometer, as well as the 30 m single-dish for positions 1, 2, 5, and 7. The optical line properties derived from Gemini, the slit positions associated with the COS beams, and the CO(1–0) line properties are gathered in Table 4. Our five pointings were also chosen to probe diverse environments. As the background HST WFC3 image in Figure 1 shows, positions 1, 2, and 7 are associated with bright Hα knots in the intragroup medium ridge, while positions 3 and 5 are not. Positions 1, 2, and 5 are associated with very broad optical line emission, with line ratios consistent with pure shock excitation (see Figure 10 in Konstantopoulos et al. 2014). Position 5 lies in the so-called bridge between NGC 7319 and the ridge, and shows faint, diffuse Hα emission filling up the COS beam, associated with NGC 7319's tidal tail. Position 3 points toward a region of the ridge devoid of compact Hα emission. The associated Gemini slit is slightly offset from the COS beam and hits a bright Hα knot, whose excitation is consistent with that of an H II region, so comparison between COS and Gemini data at this position may not be meaningful. Position 7 is located in the SQ-A starburst region in the Northern region of the ridge, and is one of the two brightest star-forming regions in the intragroup medium of SQ. This region is known to combine photoionization from star formation and shocks. Indeed, for

Table 1
MAST Archive Name, Positions, COS Gratings, Central Wavelength, and Individual Exposure Times for Each of the Five Positions Observed

COS target (MAST)	R.A. (J2000)	Decl. (J2000)	Grating	λ_{cen} [Å]	Exp. time [seconds]
HCG92-1	22 35 59.765	+33 58 21.33	G130M	1096	1287.872
			G130M	1222	1437.696
			G160M	1611	3180.512
			G160M	1623	3673.536
HCG92-2	22 36 00.032	+33 58 06.75	G130M	1096	1287.936
			G130M	1222	1437.760
			G160M	1611	3180.544
			G160M	1623	3673.568
HCG92-3	22 35 59.439	+33 58 34.80	G130M	1096	1429.056
			G130M	1222	1447.840
			G160M	1611	3180.576
			G160M	1623	3673.568
HCG92-5	22 36 01.222	+33 58 22.74	G130M	1096	1366.016
			G130M	1222	1359.552
			G160M	1611	3180.640
			G160M	1623	3671.584
HCG92-7	22 35 58.953	+33 58 49.96	G130M	1096	600.000
			G130M	1222	599.712
			G160M	1611	1102.656
			G160M	1623	1303.712

instance, optical Gemini spectra show strong variation in the Hα/N II line ratio as a function of gas velocity. In this paper, to characterize the dissipation of turbulence in the intragroup medium environment of SQ, we focus on regions known to be shock dominated.

2.2. Reduction of COS Spectroscopic Data

SQ was observed with the medium-resolution far-UV G130M (Lyα) and G160M (C IV) gratings of HST-COS on 2014 November 9 for a total of 15 orbits. Descriptions of the COS instrument and on-orbit performance characteristics can be found in (Osterman et al. 2011; Green et al. 2012), as well as in the COS Instrument Handbook. In order to achieve continuous spectral coverage across the G130M bandpass (1135–1440 Å) and to minimize fixed-pattern noise, we made observations at two central wavelength settings (1291 Å and 1300 Å) with four focal-plane offset locations in each grating setting (i.e., FP-POS = 1, 2, 3, 4). This combination of grating settings ensures the highest-signal-to-noise-ratio observations at the shortest wavelengths available to the G130M mode at a resolving power of $R = \lambda/\Delta\ \lambda \approx 16{,}000$ (about 17 km s^{-1} velocity resolution for a point source). For every sightline, COS observations yielded a continuous spectrum spanning $\lambda \approx 1150$–1800 Å. The calibration of the wavelength scale with updated dispersion solutions ensures a velocity accuracy of 7 km s^{-1}. The exposure times were chosen to achieve a signal-to-noise ratio (S/N) of 7–15 per resolution element (7 pixels, ≈0.07 Å, FWHM = 15 km s^{-1} for a point source) at $\lambda \approx 1300$ Å, depending on the velocity range. We note that the spectral resolution could be significantly lower for extended sources, as low as $R = 1450$ for G130M if the emission uniformly fills the COS beam. In particular, this may be the case for positions 3 and 5, which do not show an associated compact Hα source within the COS aperture. The target positions, grism configurations and individual exposure times are presented in Table 1. We plot the spectra binned to the standard seven pixels.

We started our data reduction from the x1d.fits files produced by the COS calibration pipeline, *CalCOS*,[14] downloaded from MAST. To assess the contamination of the spectra by geocoronal airglow lines, we have filtered the data in time in order to produce spectra utilizing only data taken during orbital night time. To do that, we used the *TimeFilter* routine from the COSTOOLS package[15] to select night-time data in the COS corrtag files, and then reextracted the data into x1d spectra. The comparison between the night-only and full data sets did not yield significant improvement because the redshift of the source (0.02) shifts the Lyα line to 1240 Å, in between the geocoronal Lyα and [O I] lines. The data have then been aligned and coadded with the COADD_X1D.pro V3.3 IDL routine provided by STScI.[16] To take into account the strong wings of the non-Gaussian, Line Spread Function (LSF) of COS, we have used the COS_LSF.pro IDL routine to produce a LSF model at the nearest tabulated wavelength value. The COS exposures for each regions were deconvolved using the LSF appropriate for corresponding grating setting and for the central wavelengths of the Lyα and C IV emission lines. The absolute flux calibration steps are described in detail in the COS data handbook,[17] and are expected to of the order of ±5% for G130M and G160M (errors are dominated by fixed-pattern noise in the UV detectors and uncertainties in the time-dependent sensitivity correction).

2.3. Visible Light IFU Spectroscopy

We also present Integral Field Unit (IFU) observations made with the George and Cynthia Mitchell Spectrograph (hereafter GCMS, formerly known as VIRUS-P) mounted on the 2.7 m Harlan J. Smith Telescope at McDonald Observatory (Hill et al. 2008; Blanc 2013). The IFU uses a 246-fiber bundle, with each fiber covering 4.″16 on the sky, which makes it sensitive to faint extended emission. We used a three-point dither pattern to completely cover the 2.82 arcmin^2 field of view, and to fill in gaps between the fibers. Observations were obtained on 1 Oct 2011 with an integration time of one hour at each of the three dither positions. We used the VP2 blue grating, which has a spectral resolution of ∼1.6 Å (∼100 km s^{-1}) and covers the wavelength range ∼4700 to ∼5350 Å. The data reduction was performed using the VACCINE software package (Adams et al. 2011), and these data were further flux calibrated using a bootstrapping method which compares each fiber response to a calibrated SDSS b-image of the galaxy (e.g., Joshi et al. 2019). Wavelength calibration was performed using lamp spectra obtained at the beginning of the observing run.

[14] see HST COS Instrument Handbook for more details: http://www.stsci.edu/hst/cos/documents/handbooks/current/cos_cover.html.
[15] https://github.com/spacetelescope/costools
[16] available at http://casa.colorado.edu/~danforth/science/cos/costools.
[17] https://hst-docs.stsci.edu/cosdhb/chapter-3-cos-calibration

3. Extremely Broad Lyα Line and Kinematics of the Ionized Medium

3.1. Individual COS Pointings: Line Fluxes and Kinematics

We detect strong and broad Lyα (1215.67 Å) emission from all the five observed regions shown in Figure 1. The Lyα line profiles for each of the 5 observed positions, shown in Figures 2(a)–(e) and 3(a)–(e) (in red), have complex, multi-peaked profiles. The observed coordinates and integrated Lyα and molecular hydrogen (H_2) line fluxes for each region are presented in Table 2. Our observations involve only a few COS sight-lines and therefore provide a sparse view of the Lyα emission across the intragroup medium. It is therefore not possible to quantify the total Lyα luminosity from the intragroup medium, and we will restrict our analysis to the comparison of line fluxes at the COS positions.

The Lyα flux averaged over the 5 COS beams amounts to ≈40% of the warm H_2 IR line emission (see last column of Table 1), which is the dominant cooling channel in the shocked intragroup medium (Appleton et al. 2017) and similar to that of the [C II] line and X-rays as well (see Table 1 in Guillard et al. 2009, for a summary of the energy budget across gas phases). Remarkably, on average, the Lyα line luminosity is comparable to that of much cooler and hotter gas, assuming that the ratio of Lyα to H_2 emissions is the same over the whole shocked intragroup medium. Section 5.3 discusses the implications of this observational result on the properties of kinetic energy dissipation in the intragroup medium of SQ. We also note that the Lyα flux varies by a factor of ≈10, between the bridge (faintest) and the ridge 1 (brightest) positions.

In Table 3, we gather our measurements of the widths of the Lyα lines for the five observed positions, as well as for the stacked spectrum. There is a large variation of the widths of the Lyα lines, with full width at zero intensity (FWZI) up to ≈2100 km s^{-1}. This is remarkable, given that the COS beam is sampling a small region of intergalactic space between the galaxies (the 2.5 arcsec beam diameter corresponds to 1.1 kpc).[18] This suggests that the COS beams likely probe the same large-scale organized structure in the filament seen at other wavelengths, rather than small individual emission regions. This becomes clear when we compare the Lyα profiles with Hβ lines, shown as red and green profiles, respectively, on Figure 2, and with [C II]157.7 μm lines (Appleton et al. 2013), shown as yellow profiles on Figure 3. In many cases, the complex Lyα profile shapes track approximately the main kinematic features from the other lines, which are known to show large-scale coherence (see for example Rodríguez-Baras et al. 2014; Duarte Puertas et al. 2019).

Figures 2 and 3 show the varying velocity, profile shapes, line widths, and strength of the Lyα emission, compared with other line profiles at the same positions. The broadest Lyα line we observed is seen in Figures 2(a) and 3(a), obtained at position HCG92-1 (see Figure 1 and Table 3), near the center of the giant H_2 emitting filament. In this profile, the Lyα emission tracks quite well the shape of the Hβ and [C II] profiles at low heliocentric velocity, but deviates strongly at higher velocities. The Lyα emission extends to at least $V_{\rm helio} = 7600$ km s^{-1}, whereas both the [C II] and Hβ emission fall almost to zero flux at velocities of no more than 7300 km s^{-1}, compared to the barycentric systemic velocity of 6600 km s^{-1}. The excess emission seen above 7300 km s^{-1} may be evidence of resonant scattering and bulk motions of the scattering medium, which is common in Lyα systems (see Section 5.2 for a discussion of the origin of the line broadening). This is supported by the observation that the line profiles, taken with both the Mitchell Spectrograph and Herschel generally occupy a more limited range of radial velocities compared with the Lyα emission, despite being taken over larger beam sampling areas than the COS data, i.e., 4×4 arcsec^2 for GCMS and 9.4×9.4 arcsec^2 for the [C II]157.7 μm line, see Appleton et al. (2013).

Other examples of possible resonant scattering wings in the Lyα profiles compared with the [C II] and Hβ emission lines are the blue wing seen in HCG-2 (Figure 3(b)) at $V_{\rm helio} < 5800$ km s^{-1} and the blue wing in HCG-5 (Figure 3(d)). In both cases, the Lyα emission extends significantly blueward of the Hβ line by velocities of up to 200–300 km s^{-1}.

3.2. Comparison with CO (1–0) Line Profiles

We compare the Lyα and Hβ lines with CO (1–0) line profiles obtained respectively with the IRAM NOEMA interferometer and the single-dish IRAM 30 m telescope (from Guillard et al. 2012), respectively, in Figures 2 and 3. Our CO (1–0) observations with the IRAM NOEMA interferometer, which will be presented in a companion paper (Guillard et al. in prep.), show giant, kiloparsec-scale molecular complexes of a few $10^8\,M_\odot$ in the shock, some of them associated with Hα-emitting regions. From the cleaned CO (1–0) line emission map, we have extracted spectra within beams centered on the COS positions, using a synthesized beam of 4.3×3.5 arcsec^2, of position angle P.A. = 100°. We used the IRAM GILDAS mapping suite of routines[19] to perform the extractions, and then exported the spectra into fits files. The line parameters are gathered in Table 2. The CO (1–0) line intensity was computed by integrating the line profile, and the central velocity and line velocity dispersion were computed after a Gaussian fit to the profile. The comparison between the CO (1–0) and Lyα line profiles is shown in Figure 2, with the caveat that the NOEMA beam is twice as large as the COS beam. It is striking that the CO lines detected with NOEMA are much narrower than the Lyα lines, except in the Northern star-forming region (SQ-A, position 7), where the main CO velocity component at 6700 km s^{-1} matches the Lyα profile. Those molecular complexes are much larger than the small-scale structure of the neutral gas through which Lyα photons scatter out of the intragroup medium. However, the spatial resolution of the NOEMA observations being 1.8 kpc, those giant molecular complexes could well break down into much smaller clumps with sometimes large shear motions between them (≈100 km s^{-1}). We also note that there may be a more diffuse, extended molecular component, which may be filtered out by the interferometer. This is illustrated on Figure 3, where we compare the Lyα and [C II] line profiles with CO(1–0) from single-dish IRAM 30 m data. In this case, the single-dish CO line profiles are much broader than the interferometric data.

3.3. Overview of the Large-scale Motions of the Intragroup Medium Gas

Part of the complexity of the Lyα line profiles can be understood when the full picture of the ionized gas (as

[18] Stephan's Quintet is assumed to be at a distance of 94 Mpc.

[19] https://www.iram.fr/IRAMFR/GILDAS/doc/pdf/map.pdf

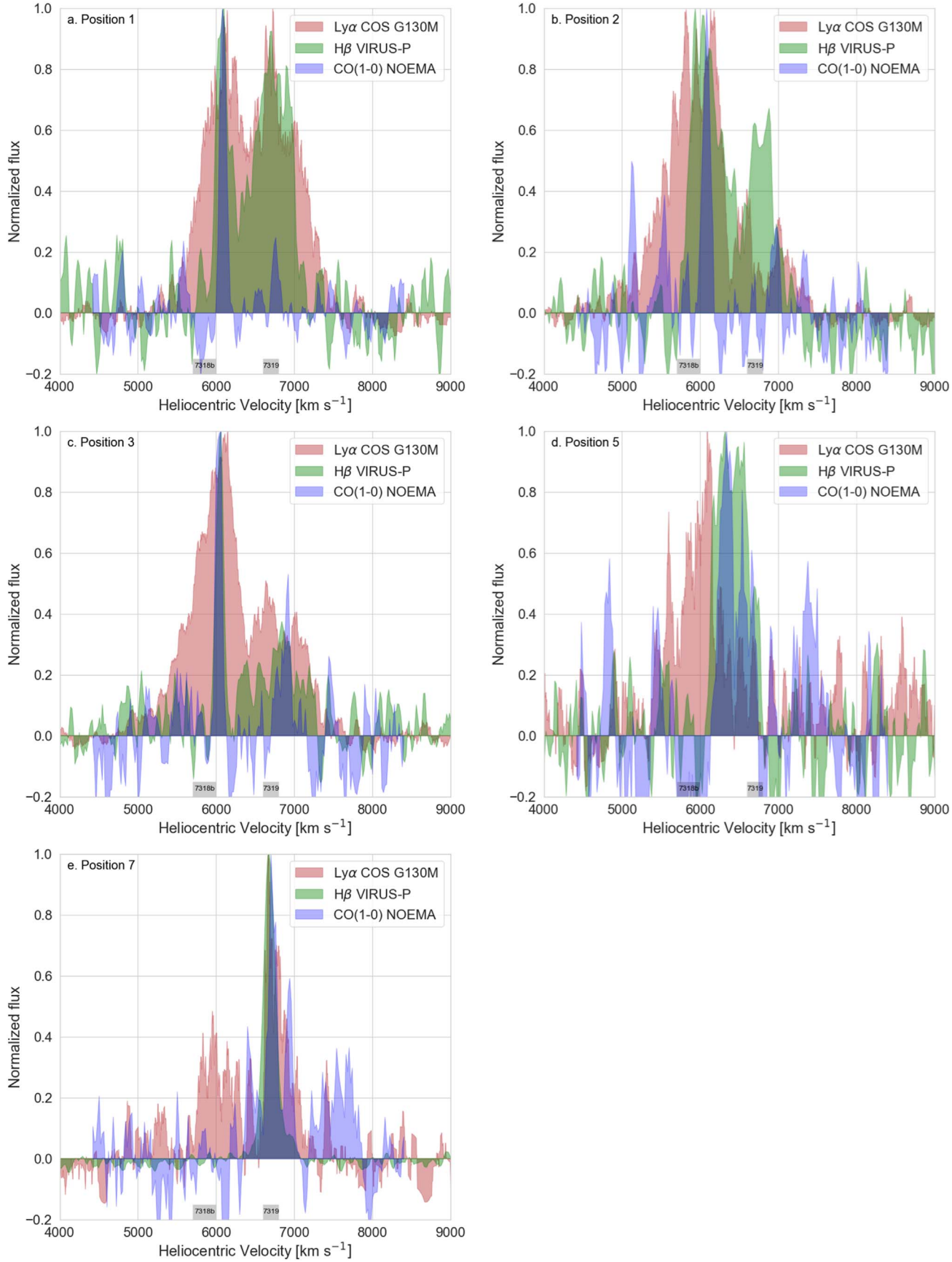

Figure 2. Comparison of Lyα (red), Hβ (green), and CO (1–0) (blue) line profiles for the five positions observed. The CO (1–0) PdBI spectra are extracted at the COS positions over an ellipsoidal beam of 4.3 × 3.5 arcsec^2, P.A = 100 degrees. The Lyα, CO(1–0), and Hβ spectra have velocity resolutions of 20, 30, and 100 km s^{-1}, respectively.

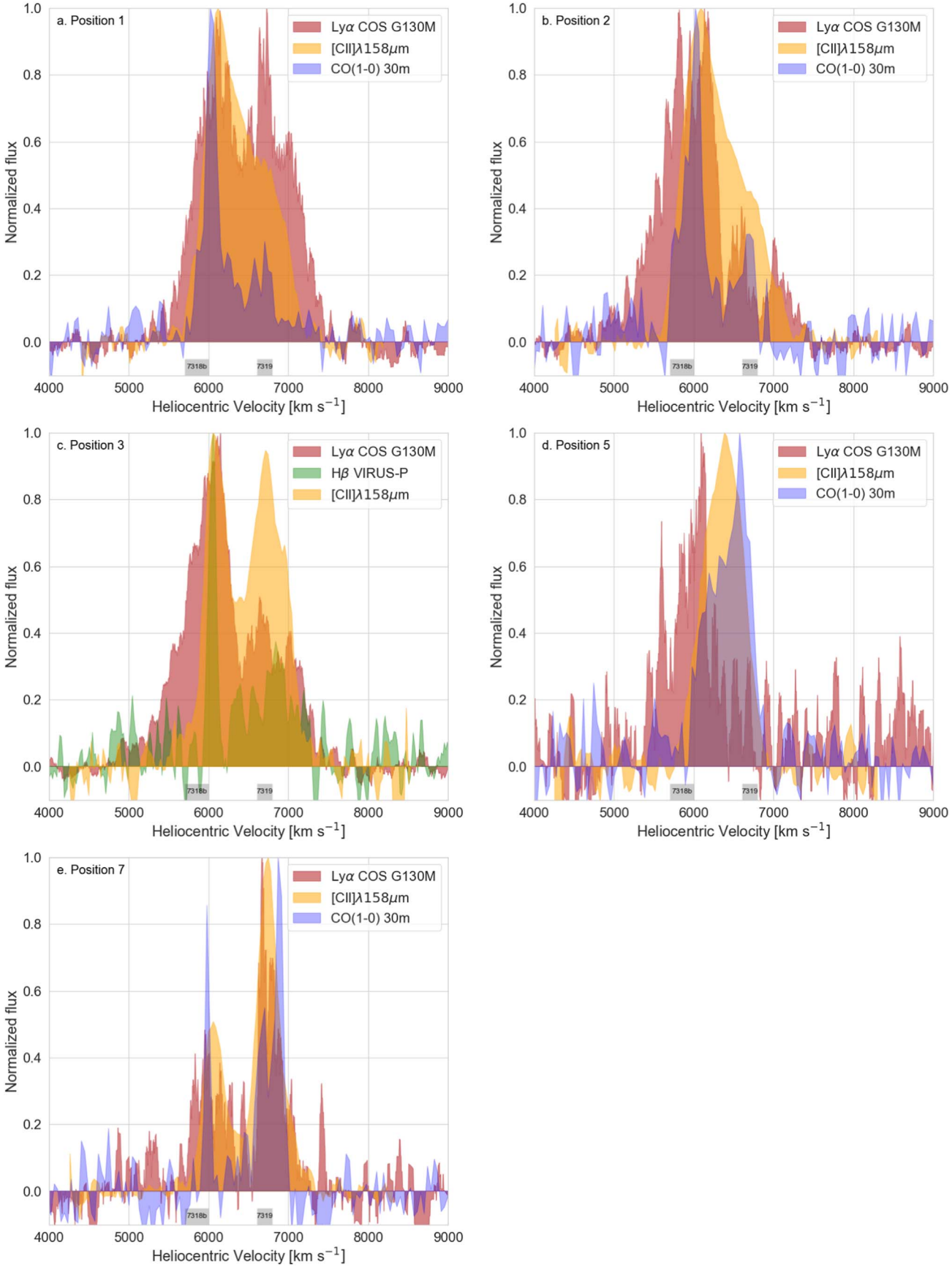

Figure 3. Comparison of Lyα (red), Herschel [C II] spectra, and IRAM single-dish 30 m CO(1–0) line profiles for the five positions observed. For position 3, where no IRAM 30 m data is available, we added the comparison to the Hβ line taken with the GCMS (VIRUS-P) IFU Spectrograph.

Table 2
Observed Lyα, Hβ, and H_2 Line Fluxes and Line Ratios for the COS Lines of Sight

COS target	$F_{Ly\alpha}$: Lyα Flux[a] [10^{-18} W m^{-2}]	$F_{H\beta}$: Hβ flux[b] [10^{-19} W m^{-2}]	F_{H2}: H_2 flux[c] [10^{-18} W m^{-2}]	$F_{Ly\alpha}/F_{H\beta}$	$F_{Ly\alpha}/F_{H2}$
HCG92-1 (ridge)	5.3 ± 0.5	1.7 ± 0.2	6.7 ± 0.8	30.9 ± 3.4	0.77 ± 0.12
HCG92-2 (ridge)	5.2 ± 0.5	2.4 ± 0.2	7.3 ± 0.9	22.0 ± 2.5	0.71 ± 0.11
HCG92-3 (ridge)	1.1 ± 0.1	1.6 ± 0.3	5.8 ± 0.7	7.0 ± 1.2	0.19 ± 0.03
HCG92-5 (bridge)	0.4 ± 0.1	0.8 ± 0.1	5.5 ± 0.6	4.7 ± 0.9	0.07 ± 0.02
HCG92-7 (SQ-A)	1.3 ± 0.1	6.7 ± 0.1	7.0 ± 0.8	1.8 ± 0.2	0.17 ± 0.02
all (stacked)	13.3 ± 0.2	13.2 ± 0.4	32.3 ± 1.7	10.1 ± 1.4	0.41 ± 0.03

Notes.
[a] Uncorrected for Lyα absorption. Some of the profiles show evidence of absorption (see text).
[b] Sum of the observed line flux estimated on a 4×4 arcsec^2 square aperture from the Mitchell Spectrograph IFU data, scaled to the circular COS aperture of 2.″5 in diameter assuming constant surface brightness.
[c] Sum of the (0-0) S(0) + (0-0) S(1) + (0-0) S(2) + (0-0) S(3) pure rotational H_2 line fluxes derived from extractions of 5.5×5.5 arcsec^2 from Spitzer IRS data (Appleton et al. 2017), scaled down to the circular COS aperture of 2.″5 in diameter assuming constant surface brightness.

(This table is available in its entirety in machine-readable form.)

Table 3
Observed Lyα Line Kinematical Properties for the COS Lines of Sight

COS target	W_{10}(Lyα)[a] [km s^{-1}]	W_{20}(Lyα)[a] [km s^{-1}]	W_{50}(Lyα)[a] [km s^{-1}]
HCG92-1	1910 ± 40	1690 ± 20	1290 ± 40
HCG92-2	2120 ± 40	1080 ± 20	690 ± 20
HCG92-3	2000 ± 40	1770 ± 20	570 ± 20
HCG92-5	1120 ± 40	930 ± 40	350 ± 20
HCG92-7	1480 ± 40	530 ± 40	220 ± 20
all (stacked)	2650 ± 40	1820 ± 20	595 ± 15

Note. W_{10} has been computed after smoothing the spectra to 80 km s^{-1} to increase the SNR in the line wings, and is close to the full width at zero intensity of the line. In case of the presence of several velocity components, only the widest component is listed.
[a] Widths at 10%, 20%, and 50% of maximum flux.

measured optically) is explored. Other authors have presented two-dimensional spectral maps of the optical emission lines in Stephan's Quintet (Iglesias-Páramo et al. 2012; Konstantopoulos et al. 2014; Rodríguez-Baras et al. 2014; Duarte Puertas et al. 2019), but we will use our own data from the GCMS spectrograph to provide an overview and context for the observed profiles. In Figure 4, we show a sequence of representative Hβ surface-brightness emission maps for the inner SQ group. For context, the radial velocity of the intruder galaxy, NGC 7318b is $V_{sys} = 5774$ km s^{-1}, and it is thought to be entering the group from behind with a blueshifted discrepant velocity of almost 1000 km s^{-1} relative to the rest of the group members and the group-wide gas (Xu et al. 2003; Hwang et al. 2012). A component of the ionized gas (Figures 4(a) and (b)) follows the spiral arm and H II regions seen in NGC 7318b, as expected if some of the gas was part of that galaxy. Gas is also seen from the nucleus and northern disk of NGC 7319, (Figures 4(c), (d) and (e)), but with significant emission from the main North-South shocked filament. Gas at intermediate velocities (Figures 4(c) and (d)) is spread along the filament, but also in the bridge between NGC 7318b and NGC 7319. The bridge is fragmentary in nature at Hβ and occupies a narrower range of velocities compared with the main filament. The pile-up of gas with such a wide range of velocities along such a narrow structure in the main filament is a unique and remarkable feature of the Stephan's Quintet system.

3.4. Stacked Spectra and the Detection of the CIV$\lambda\lambda$1548, 1550 Å Doublet

In Figure 5 we show the averaged spectra of both Lyα and the CIVλ1549 Å line, stacked over the five observed positions. We found all ten G160M integrations setting (two wavelengths per position) free of strong fixed-pattern noise features and thus suitable for co-addition. The CIV line detected on the stacked spectra is centered around the heliocentric recession velocity of the intragroup gas ($\approx$6000 km s^{-1}) and is very broad (FWHM $>$ 1000 km s^{-1}). The profiles of the stacked Lyα and CIV lines also show some similarities, with, for Lyα, a brighter low-velocity component around 6000–6200 km s^{-1} and a fainter shoulder around 6300–7000 km s^{-1}. We note that the noise in the stacked spectrum is not Gaussian, indicating that some low-level pattern noise is present, which makes the estimate of the S/N of the line uncertain. The individual spectra are not very useful and show weak detections ($\approx 2\sigma$) for all five positions.

4. Absorption and Scattering of Lyα Photons in the Intragroup Medium

By comparing the Lyα, Hβ, [C II] and CO spectra, we can deduce at which velocities along the line of sight the Lyα photons are mostly absorbed. Generally speaking, looking at Figures 2 and 3, the Lyα and [C II] profiles are sometimes closer in shape than Lyα and Hβ. This result recalls the work of Appleton et al. (2013) showing that most of the [C II] line emission is associated with the warm ($T > 100$ K) molecular gas (H_2), and that the [C II] emission cannot be accounted for by recombination in the warm ionized medium. Therefore, both [C II] and Lyα trace gas that is heated by mechanical energy dissipation.

There are four possible examples of where Lyα absorption is taking place. In Figures 3(b) and (c) we see that the high-velocity component of the double profile seen in both Hβ and [C II] is significantly suppressed compared with the low-velocity component. For Figure 2(b) in particular, the peak in the Hβ profile falls close to a strong dip in the Lyα profile, which appears as two small wings on either side of the dip. For Figure 3(c), the feature seen in both [C II] and Hβ is largely suppressed above 6500 km s^{-1}. Also, in Figures 2(d) and 3(d), the Lyα profile is shifted blueward of the main [C II] and Hβ peaks, suggestive of absorbing gas centered at

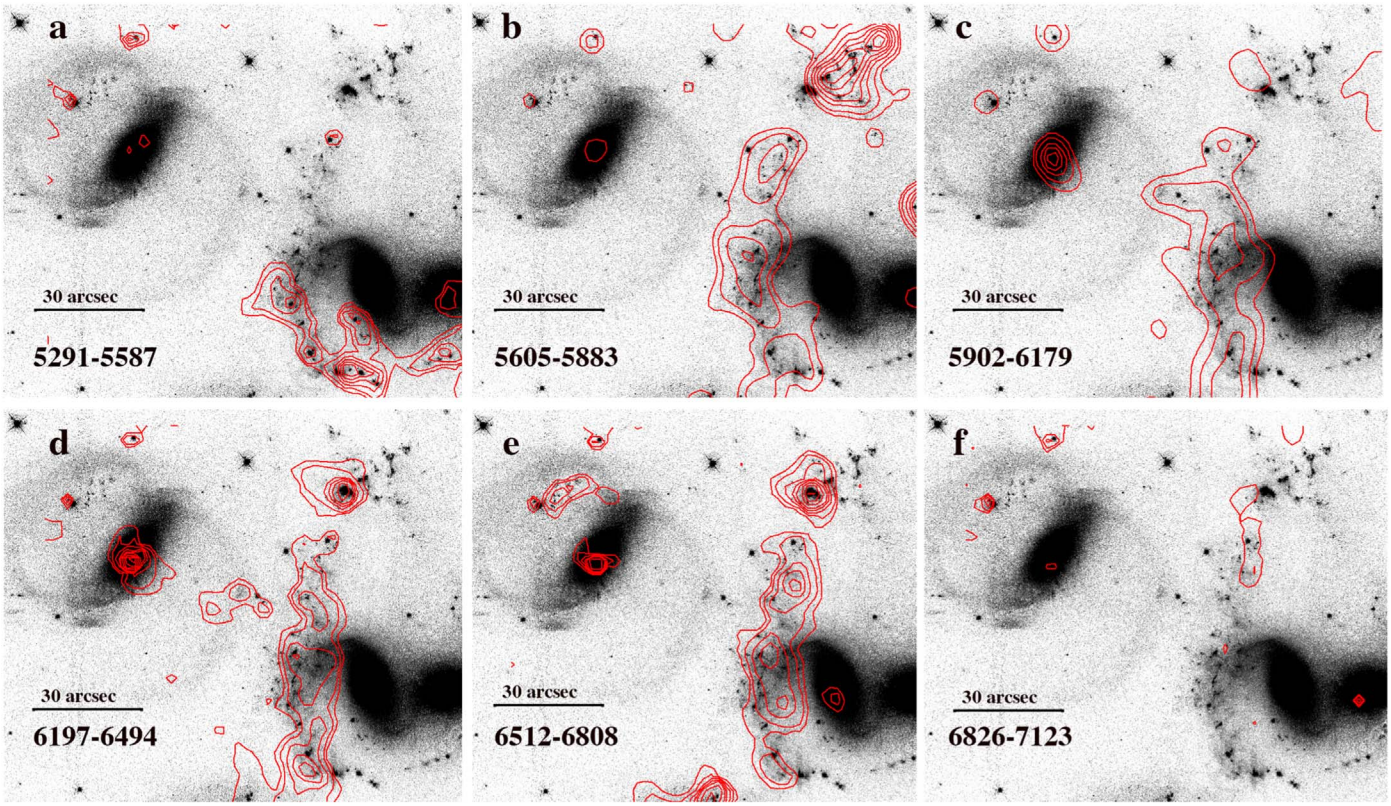

Figure 4. Contours of Hβ surface brightness emission (in red) from Stephan's Quintet based on the Mitchell Spectrograph observations covering the full range of heliocentric velocities from 5291 to 7123 km s^{-1} in which emission was detected. Each subfigure (a to f) shows the integrated surface brightness of the emission in units of 2.5, 5, 10, 15, 20, 25, 30, 40, 50, and 60 $\times$ 10^{-18} erg s^{-1} cm^{-2} arcsec^{-2} over the range of velocities indicated. Subfigure (b) covers the velocity range that includes the intruder galaxy (V_{sys} = 5774 km s^{-1}), whereas the barycenter of the group (V_{sys} = 6600 km s^{-1}) is represented in panel (e). Gas is also seen at intermediate velocities in the bridge between the main filament and the Seyfert galaxy NGC 7319 (panels (c) and (d)). Note a possible outflow from NGC 7319. All of the contours are projected against the HST WFC3 F665N (Hα) greyscale image of the system.

Table 4
CO (1–0) Line Properties Extracted at the Positions of the COS Apertures and Optical Line Properties

COS target	I_{CO}[a] [Jy km s^{-1}]	v_{CO}[a] [km s^{-1}]	σ_{CO}[a] [km s^{-1}]	Gemini Id[b]	F(Hα)[c] [10^{-18} W m^{-2}]	[NII]/Hα[c]	[O I]/Hα[c]	Hβ/Hα[c]
HCG92-1 (ridge)	2.6 ± 0.2	6084.9	28.8	15053*	0.0774 ± 0.0058	0.168 ± 0.001	0.251 ± 0.002	0.320 ± 0.002
HCG92-2 (ridge)	1.8 ± 0.2	6080.1	30.6	12002	0.2553 ± 0.0180	0.141 ± 0.001	0.203 ± 0.002	0.145 ± 0.003
HCG92-3 (ridge)	2.2 ± 0.3	6260.0	35.7	14006*	0.0639 ± 0.0016	0.129 ± 0.001	0.025 ± 0.001	0.241 ± 0.001
HCG92-5 (bridge)	1.1 ± 0.3	6350.0	67.8	20001	0.0276 ± 0.0007	0.210 ± 0.002	0.217 ± 0.001	0.460 ± 0.002
HCG92-7 (SQ-A)	4.3 ± 0.3	6736.8	19.8	30109	1.0383 ± 0.0032	0.051 ± 0.001	0.217 ± 0.001	0.197 ± 0.002

Notes.
[a] Parameters estimated from the CO (1–0) spectrum extracted from the IRAM NOEMA interferometer data (Guillard et al. in prep.) on a beam size 4.2 × 3.9 arcsec^2: integrated intensity, central velocity, and velocity dispersion.
[b] Closest Gemini slit ID from Konstantopoulos et al. (2014). The star indicates when the Gemini slit is slightly offset from the COS aperture.
[c] Hα flux and optical line ratios from Konstantopoulos et al. (2014).
(This table is available in its entirety in machine-readable form.)

V_{helio} = 6500–6700 km s^{-1}. Asymmetric Lyα profiles like this are often associated with radial outflows in galaxies (e.g., Heckman et al. 2011). The COS pointing (HCG92-5) samples the gas in the so-called "AGN bridge" (Cluver et al. 2010), a linear H_2 filament that is apparently separate from the main collisional shock in SQ. A strong shear in the velocity field of the [C II] emission was noted by Appleton et al. (2013) in that region. The spectrum of the CO (1–0) emission from that direction (see Figures 2(d) and 3(d)) shows significant CO emission at the high-velocity side of the profile, which would be consistent with absorption. Finally, HCG92-7 shows, in Figure 3(e), the opposite effect. In this case, again considering the high-velocity component of the double-horned profile only, we see that the Lyα is significantly redshifted with respect to the Hβ emission, with a sharp drop in emission as one approaches the peak of the Hβ (around V_{helio} = 6600–6700 km s^{-1}). This may be another example of asymmetric absorption, with resonant scattering to the red side of the wings of the kinematics. In summary, we see that two regions in the main emission-line filament are almost free of absorption, whereas other regions show strong absorption. Even in those cases, at least some of the Lyα emission is able

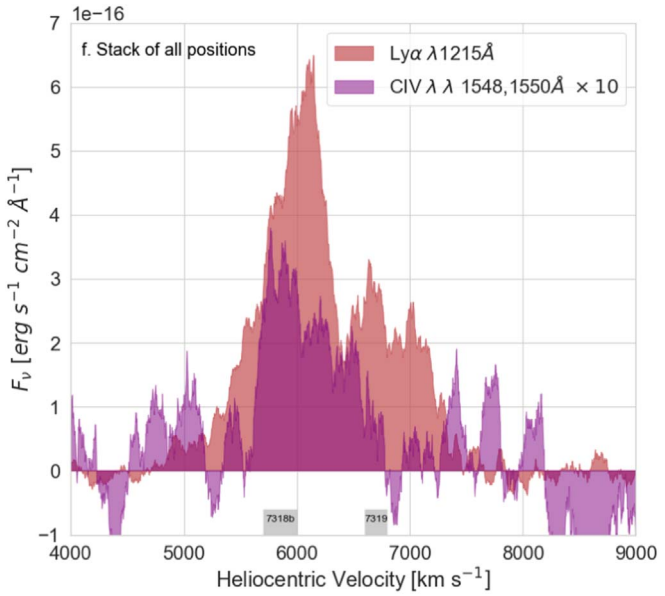

Figure 5. Lyα line (red, grism G130M) and CIV doublet (purple, grism G160M) HST COS spectra stacked over all 5 observed positions in the intragroup medium of Stephan's Quintet. The flux of the CIV line has been multiplied by a factor of 10 for clarity. The widths at 20% and 50% of the stacked CIV peak flux are, respectively, 1100 ± 60 and 900 ± 40 km s^{-1}.

to resonantly scatter and undergo many scatterings within the gas before eventually escaping into the wings of the velocity profile, where the optical depth is much lower. In Section 5.2, we estimate the escape fraction of the Lyα photons and the number of scatterings, and we discuss the multiphase structure of the intragroup medium gas. We also remind that the differences between the Lyα and Hβ spectral profiles may not only be due to Lyα scattering, because collisional excitation could also contribute.

Does this interpretation make sense in terms of the expected line ratios for the hydrogen lines? In Table 2 we also present the Hβ line fluxes and Lyα to Hβ flux ratios integrated over the 5 different sets of spectra. It is interesting that HCG92-1 and 2 both show ratios (31 and 22, respectively) consistent with little or no absorption when compared with Case B recombination (Case B predicts for $T = 10^4$ K and typical interstellar densities a flux ratio F(Lyα)/F(Hβ) of $\sim$33). The lack of extinction inferred from the line ratio for HCG-1 is entirely consistent with our previous description of the close similarity between the Lyα and Hβ line profile shapes. The slightly lower Lyα-to-Hβ ratio is consistent with the increased absorption in the red component of the Lyα profile. For both HCG92-3 and 5, F(Lyα)/F(Hβ) are significantly lower than Case B, suggesting stronger absorption, which is again consistent with the line profiles. Finally, HCG92-7, which is associated with the extragalactic HII regions and contains significant star formation and dust, shows the highest deviation from Case B (F(Lyα)/F(Hβ) $\sim$2) suggesting that, at that position, most of the Lyα photons are absorbed by dust.

5. Origin and Properties of the Lyα Emission in the Intergalactic Medium of SQ

5.1. Shocks and Turbulent Mixing Layers

Strong Lyα line emission, with typical FWHM of 200–1500 km s^{-1}, is often observed in high-redshift galaxies (e.g., Tapken et al. 2007), where Lyα photons produced by powerful starbursts scatter off neutral gas carried in outflows. Similar broad Lyα profiles are sometimes seen in the inner regions of Lyα nebulae associated with luminous high-z quasars (e.g., Ginolfi et al. 2018). However, these extreme conditions are the antithesis of those seen in the SQ filament, where the star formation activity is very weak and, globally, the Lyα emission is mainly powered by dissipation of mechanical energy. In this section, we argue that both radiative shocks and turbulent mixing layers may contribute to powering the observed Lyα line emission.

Shocks having velocities high enough to reach temperatures capable of collisionally exciting electronic states of atomic hydrogen (above 10^4 K) are a strong source of Lyα photons (e.g., Shull & McKee 1979; Dopita & Sutherland 1996; Lehmann et al. 2020). Due to collisional ionization of hydrogen, Lyα and Hβ photons are mostly produced in gas at temperatures smaller than $T = 10^5$ K, with collisional excitation dominating recombination for $T > 10^4$ K (Raga et al. 2015). In the intragroup medium of SQ, it is likely that a wide distribution of shock velocities is present (Guillard et al. 2009). In this paper we do not attempt at a detailed modeling of the line emission from shocks. We rather aim at qualitatively determining which shocks contribute the most to the Lyα and CIV line emission.

To do so, we use the results from the MAPPINGS V shock code library. The physics of the models is fully described in Sutherland & Dopita (2017) and the data in Alarie & Morisset (2019). These shock models are based on Allen et al. (2008), but the new models extend the predictions for shocks and radiative precursors to shock velocities smaller than 100 km s^{-1}, as well as up to 1500 km s^{-1}. These models include expanded atomic cooling lines and comprise a wide range of shock precursor conditions, from completely neutral gas through partially ionized and fully ionized. Magnetic fields are also included as they can strongly impact the compression and temperature of the post shocked gas. Figure 6 shows results from the MAPPINGS V shock models for a neutral atomic preshock gas with density $n_{\rm H} = 10$ H cm^{-3} and a preshock magnetic field intensity of $B = 1\,\mu$ G. The preshock gas ionization fraction is computed from the UV emission generated by the shock. We only show models for shock velocities above $V_s > 50$ km s^{-1} because modeling of H_2 line emission shows that, in SQ, lower velocity shocks are molecular shocks (Guillard et al. 2009).

The left panel of Figure 6 shows some optical and UV lines fluxes normalized[20] to ρV_s^3, i.e., the sum of the kinetic and enthalpy fluxes, where $\rho = 1.4\, n_{\rm H} m_{\rm H}$ is the gas mass density as a function of the shock velocity V_s. The solid lines show the fractional line luminosities from the shock only, while dashed lines include the contribution of the precursor for shock velocities $V_s > 100$ km s^{-1}. Due to collisional ionization of hydrogen atoms, the fraction of the shock emission accounted for by Lyα photons is the highest for shock velocities smaller than 100 km s^{-1}, for which hydrogen excitation is mainly collisional. Faster shocks do contribute to Lyα emission but to a lesser fraction of the total radiated power. For shock velocities typically above 150 km s^{-1}, the Lyα shock emission comes mainly from the photoionisation of the postshock gas

[20] See the energy conservation equation Equation (4) in (Allen et al. 2008). For negligible magnetic energy, the total radiative flux of the shock is $F_{\rm tot} = 0.5\rho V_s^3$.

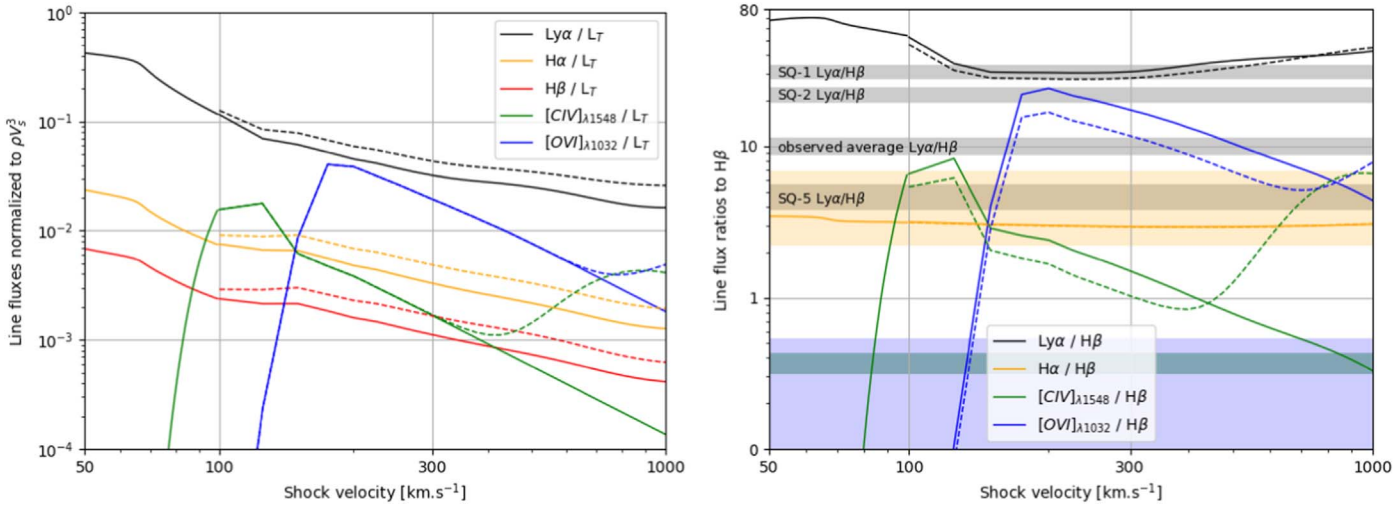

Figure 6. Results from the MAPPINGS V shock models library from Alarie & Morisset (2019), covering a range in velocities of 50–1000 km s^{-1}. Solid lines show the contribution of the shock only and dashed lines include the contribution of the radiative precursor at velocities $V_s > 100$ km s^{-1}. In this grid of models, the preshock Hydrogen density is $n_{\rm H} = 10$ H cm^{-3} and the preshock magnetic field intensity is $B = 1$ μ G. *Left:* Line fluxes normalized to $\mu m_H n V_s^3$ as a function of the shock velocity V_s. $\mu = 1.3$ is the mean molecular weight for neutral gas, and $m_{\rm H}$ the atomic mass unit. For weakly magnetized shocks like those presented here, ρV_s^3 is close to the total radiative flux of the shock. *Right:* Line emissivity ratios to Hβ flux vs. shock velocities, with the same chemical abundances (Solar) and shock parameters as Allen et al. (2008). The gray bands show Lyα/Hβ ratios for the three positions (1, 2, and 5) associated to broad optical line emission and shock excitation, and the value averaged over all positions (see Table 4). The orange and green bands show, respectively, the range of observed Hα/Hβ ratios and the stacked CIV/Hβ value with a ±20% uncertainty. The blue band shows the 3σ upper limit on the OVI/Hβ ratio.

that has cooled down to $\sim 10^4$ K. The UV emission produced in fast shocks is also in part processed into Lyα photons by hydrogen photoionization in the radiative precursor (Sutherland & Dopita 2017). The CIV and OVI line fractions peak at shock velocities higher than for Lyα, 120, and 200 km s^{-1} respectively. The contribution of photoionization to the Lyα emission could thus be significant in the intragroup medium of SQ. This contribution would still be associated with the dissipation of mechanical energy, since, in SQ, the UV flux is mostly produced by shocks.

In the right panel of Figure 6, we show model predictions for the strength of various emission line fluxes normalized to the Hβ line, and we compare them to the observed values, averaged for the five positions. The Hα/Hβ ratio in the models is always above the case B value (2.86) and slightly below the stacked value (Hα/Hβ = 4.3), although observations toward the five positions span a large range, i.e., Hα/Hβ = 2.2–6.9. The rise of the Lyα/Hβ at low velocities ($V_s < 150$ km s^{-1}) is due to collisional excitation in the postshock gas, since the precursor gas entering the shock is neutral (Sutherland & Dopita 2017). We also note that both the low CIV/Hβ observed ratio and the OVI/Hβ upper limit[21] point to shocks below 150 km s^{-1}.

Another contribution to the generation of Lyα emission could be irradiated molecular shocks at lower velocities than those presented in Figure 6. Shocks at velocities 30–50 km s^{-1} driven into molecular gas at typical densities $n_{\rm H} = 10^4$ cm^{-3} produce a strong Lyα radiation (Lehmann et al. 2020). However, the Lyα/ L_T ratio in such molecular shocks is lower (10%–20%) than for the shocks in atomic gas at similar velocities presented in Figure 6. In addition to shocks, turbulent mixing of gas phases is likely to contribute to the emission of UV line emission (e.g., Slavin et al. 1993; Kwak & Shelton 2010) and to the overall energy dissipation in the multiphase medium of SQ. Turbulent mixing layers may also explain the high CIV/ OVI line flux ratio (>0.7), akin to what is observed in the circumgalactic medium (e.g., Shull & Slavin 1994; Fox et al. 2011).

5.2. Scattering of Lyα Photons in a Highly Clumpy Medium with Large Bulk Motions as a Source of Line Broadening

Neufeld (1991) and Charlot & Fall (1993) first emphasized the impact of clumping and the multiphase nature of astrophysical media on the Lyα line strength and spectral shape. This paper does not attempt at a quantitative modeling of the Lyα emission in the multiphase intragroup medium of SQ. We only present some qualitative suggestions within the framework of Lyα radiative transfer in a clumpy medium (Zheng & Miralda-Escude 2002; Verhamme et al. 2015; Gronke et al. 2016, 2017).

Mean ratio between Lyα and Hβ fluxes measured on stacked spectra ≈10 (Table 2) may be compared with the intrinsic value ≈30 for hydrogen recombination at temperatures of a few 10^4 K and ≈80 for collisional excitation in the lowest-velocity shocks ($V_s < 100$ km s^{-1}) in the right plot of Figure 6. From this comparison, we estimate the escape fraction of Lyα photons to be ∼10%–30%. This is an effective value that varies significantly among regions and within regions with gas velocity.

In an interacting system like SQ, coherent gas flows within the SQ intragroup medium are likely to contribute to the broadening of the Lyα line profile. In particular, it is likely that the prominent blueshifted scattering wings observed at Positions 2, 3, and 5 are the result of systematic velocity gradients related to the 3D geometry of the collision between the intruder and the intragroup medium. More generally, the width of the Lyα line does not provide a direct constraint on the number of scatterings and the gas clumping. Further, existing models of Lyα radiative transfer based on microturbulence (pure random motions) make simplifying assumptions that

[21] Computed with a 3σ upper limit on the OVI line flux measured on the G130M stacked spectrum.

probably do not apply to SQ. With this caveat in mind, we provide here some indicative numbers based on these models.

In a static medium, the number of scatterings N_{sc} can be estimated from the observed frequency shift $\Delta\nu = \nu - \nu_0$, where ν and ν_0 are the observed and rest frequencies of the Lyα line, as the following: $N_{sc}^{1/2} = \Delta\nu/\Delta\nu_D \approx (a\tau_0)^{1/3}$, where $\Delta\nu_D$ is the thermal Doppler broadening, a the damping parameter, and τ_0 the line-center optical depth (see Neufeld 1990). Assuming $T = 10^4$ K and a typical velocity shift of 100 km s^{-1}, we find $N_{sc} \approx 60$. In a multiphase medium, the Lyα escape fraction $f_{\rm esc}$ depends on the dust optical depth of the clumps, τ_d, and the covering factor f_c, i.e., the average number of clumps along the sightline (Neufeld 1991). Both the modeling of the dust emission in SQ (Natale et al. 2010; Guillard et al. 2010) and studies of the molecular gas content (Guillard et al. 2012; Appleton et al. 2017) converge to an average column density of $N_H \approx 2 \times 10^{20}$ cm^{-2} in the ridge, which translates into $\tau_d \approx 0.5$ at $\lambda = 1216$ Å. Following Hansen & Peng Oh (2006) and Gronke et al. (2017), we find a covering factor $f_c \approx 15$ for a fiducial escape fraction $f_{esc} = 0.15$, and $N_{sc} \approx 80$. To test these estimates, more realistic radiative transfer models including coherent gas velocity gradients would be needed, as well as very high spatial resolution observations to confirm their presence.

In conclusion, this high escape fraction, combined with the spectral evidence of Lyα scattering, reflects the clumpy picture that has emerged from the analysis of SQ observations, mainly the spatial correlation between the tracers of the hot, warm and cold intragroup medium phases, and the modeling of the SQ dust emission (Guillard et al. 2010). The neutral gas (dominated by dusty molecular gas in the ridge) is in clumps with a high-velocity dispersion and large velocity gradients. The clumps are embedded in a hot X-ray-emitting, dust-free plasma. Within such a clumpy medium, Lyα photons may escape through multiple scatterings off the clump surfaces (Neufeld 1991; Gronke et al. 2017) without being absorbed in the interclump dust-free plasma. The clumps must fill a small fraction of the volume but their surface filling factor must be close to unity with multiple clumps along a given line of sight. Further work is needed to model these observations and to assess whether the differences in spectral shapes observed for the five pointings could be accounted for by variations in the total column of dusty neutral (molecular) hydrogen, the number of clumps along the line of sight and their kinematics. Note that not only scattering effects but also collisional excitation could also contribute to explain the differences between the Lyα and Hβ spectra.

5.3. A Constant Dissipation Rate Across Many Orders of Magnitude in Gas Temperatures: A Signpost of a Turbulent Cascade?

The observations presented in this paper brings another piece to the cooling budget puzzle of the SQ shocked intragroup medium. Putting together multiwavelength line spectroscopy allows us to combine radiative tracers that span a wide range of gas temperatures, from $\gtrsim$100 K for rotational H_2 and [C II] lines to 5×10^6 K for X-rays. Remarkably, over more than four orders of magnitude in temperature, the powers radiated by the multiphase intragroup medium in X-rays, Lyα, H_2, and [C II] are comparable within a factor of a few (see also Table 1 in Guillard et al. 2009, for a summary of the energy budget across gas phases). This indicates that the dissipation of the kinetic energy in the SQ galaxy-wide collision involves all gas phases. Dissipation could proceed through shocks with a wide distribution of velocities and involve turbulent mixing layers. Shocks and mixing layers can be the combined result of the turbulent energy cascade within the multiphase intragroup medium. While a specific probability distribution function of shock velocities is required to make the cooling rate independent of the gas temperature, models suggest that this may be a generic property of energy dissipation in turbulent mixing layers (Ji et al. 2019).

6. Similarities with the Circumgalactic Media of Distant Galaxies

The nature of the emission from the intragroup medium of Stephan's Quintet may have implications for our understanding of the observations and nature of the circumgalatic medium (CGM) surrounding galaxies in the distant universe. Superficially, there are many similarities between the CGM of galaxies and the intragroup medium in SQ. The CGM of distant galaxies have evidence for: (1) bright Lyα emission with broad lines ($\sigma \approx 100$–500 km s^{-1}) and line profiles that range from simple Gaussians, double-horned, to those with strong asymmetries (e.g., Leclercq et al. 2017; Vernet et al. 2017; Leibler et al. 2018; O'Sullivan et al. 2020); (2) emission at a wide range of frequencies, implying that the gas in the CGM is multiphase and contains cold gas (e.g., Emonts et al. 2016, 2018, 2019; Falkendal et al. 2021); and (3) line ratios of the UV and optical emission lines that are about the values expected for recombining, clumpy gas (Leibler et al. 2018; Cantalupo et al. 2019; Marino et al. 2019). The intragroup medium of SQ is also somewhat reminiscent of the very broad, shock-powered Lyα and CH^+ emission detected outside galaxies in the distant galaxy group SMMJ02399 at $z = 2.8$ (Vidal-García et al. 2021). In all of these ways, there are similarities with the selected regions of the intragroup medium of SQ we have studied.

Of particular interest is the comparison of the Hα and Lyα line ratios and surface brightnesses between the intragroup medium of SQ and the ICM of the Slug Nebula and MRC 1138-262 (Leibler et al. 2018; Shimakawa et al. 2018). In the Slug Nebula and the medium surrounding the radio galaxy, MRC 1138-262, the Lyα to Hα line ratios are about 6 and a few, respectively. These ratios are quite similar to the range of values spanned in the spectra of the regions of the SQ, less than 1 to almost 10. It is also worth noting that in the case of the Slug Nebula, the Hα line is consistent with being much narrower than the Lyα emission over the same region (Leibler et al. 2018) and similar to our findings. These results suggest that a fraction of the Lyα escapes the nebulae and that scattering plays an important role in shaping the line profiles. The surface brightness of the hydrogen lines is also quite different in these objects. In both the Slug and MRC 1138-262, the surface brightness of Hα is approximately 1–2 orders of magnitude higher than in the emission line regions we have observed in SQ. The Slug Nebula has a lower surface brightness than MRC 1138-262 but was also estimated at a much larger distant from the QSO than that used for MRC 1138-262 (estimated at the faintest surface brightness levels in the narrowband imaging data; Shimakawa et al. 2018).

Since both the Slug and MRC 1138–262 have been observed in CO transitions, we can also compare their molecular gas

surface densities. Over roughly the same regions are those used to estimate the Hα surface brightnesses, the Slug has upper limits to its H_2 gas mass surface densities, <12–25 $M_\odot$ pc^{-2} (Decarli et al. 2021), while MRC 1138–262 is about 35 $M_\odot$ pc^{-2} (Emonts et al. 2016). The mass surface densities of H_2 for SQ range from about 10–100 $M_\odot$ pc^{-2}. It is interesting that the molecular gas surface densities of MRC 1138–262 are similar while the Hα (and given the similar ratios, the Lyα) surface brightnesses are so different. This can simply be explained within the context of our analysis that both objects have strong energy injection into their circumgalactic media (a collision and a high-power radio jet), which drives a turbulent cascade, but MRC 1138–262 hosts a powerful, UV-luminous AGN that powers its optical emission line gas. The emission from the Slug Nebula is consistent with that expected from photoionized gas (Decarli et al. 2021), while clearly this is not the case for either the regions of SQ and MRC 1138–262. The injection of mechanical energy into their circumgalactic media plays an important role in shaping what we observe, especially in creating and sustaining dense molecular gas.

7. Conclusions

We have used the COS spectrograph on HST to observe Lyα emission from the intergalactic gas in SQ. The observations sample five positions across the 30 kpc wide shock. The HST data is compared with CO, [C II], and Hβ spectra. We summarize the main observational results and outline our interpretation of the data.

We detect extremely wide Lyα lines with a full width at zero intensity of ≈2000 km s^{-1}, which exceeds the velocity range of CO, [C II], and Hβ line emission. After stacking of the five HST spectra, we also detect the CIV doublet. We observe significant variations in the Lyα/Hβ spectral ratio between positions and velocity components. From the mean line ratio averaged over positions and velocities, we estimate the mean escape fraction of Lyα photons to be ∼10%–30%. The Lyα lines are systematically broader than the Hβ ones at the same positions, which we consider as observational evidence for scattering of Lyα photons by the SQ intragroup medium. The difference in velocity spread is asymmetrical and amounts to ≈300 km s^{-1} for the blueshifted Lyα wings observed at three of the five positions.

The observations provide insight on the structure of the multiphase intragroup medium in SQ. The high Lyα escape fraction and scattering reflect the clumpy picture suggested by the spatial correlation between the tracers of the hot, warm, and cold phases of the SQ intragroup medium. The neutral, mainly molecular, gas is in clumps embedded in the X-ray-emitting, hot, and dust-free plasma. Lyα photons must escape through multiple scatterings off the clumps. Scattering indicates that the intragroup medium is not porous to Lyα photons, i.e., the neutral gas surface filling factor must be close to unity with multiple clumps along a given line of sight. A quantitative comparison with Lyα radiative transfer models is beyond the scope of this observational paper, but these data suggest that coherent gas flows within the SQ intragroup medium contribute to the broadening of the Lyα line profile. In particular, it is likely that the blueshifted scattering wings follow from systematic velocity gradients related to the 3D geometry of the collision between the intruder and the SQ intragroup medium.

The bulk of the Lyα emission must be powered by dissipation of mechanical energy because the SQ star formation rate is small and the gas velocities span an exceptionally large range. This conclusion is in line with optical line ratios measured at our COS pointings. Lyα photons are emitted by gas at temperatures smaller than the thermal energy threshold for collisional ionization ($T < 10^5$ K). It is likely that both collisional excitation and recombination of photoionized Hydrogen contribute to the observed emission. Due to collisional ionization of hydrogen atoms, the fraction of the shock emission accounted for by Lyα photons is the highest for shock velocities smaller than 100 km s^{-1}. Faster shocks do contribute to Lyα emission but to a lesser fraction of the total radiated power. The UV emission produced in fast shocks is in part processed into Lyα photons in the postshock and the preshock gas. This contribution of photoionized gas to the Lyα emission, which is also associated with dissipation of mechanical energy, could be significant.

The HST observations complement our view at the energetics of the galaxy-wide shock created by the collision of a high-speed intruder galaxy with the SQ intragroup medium. The total power emitted in the Lyα line is comparable to that of much cooler gas in the mid-IR rotational $H_2$and the [C II] fine structure lines. The energy radiated in [C II], H_2, Lyα and X-rays represents cooling from gas spanning four order of magnitudes in temperature from 100 to 10^6 K. The observed fluxes are comparable within a factor of a few, which indicates that roughly the same fraction of energy is dissipated per logarithmic bin of temperature. This is a remarkable result that constrains models of the turbulent energy cascade in SQ. It emphasizes the possible contribution from turbulent mixing layers to energy dissipation.

Following the trail of mechanical energy dissipation and gas kinematic in the turbulent gas on scales smaller than ≈1 kpc (the COS aperture scale) will be possible with observations of warm molecular and ionized gas with the James Web Space Telescope and future UV-optimized telescopes. Such observations will also to look for coherent anisotropic gas flows, which are necessary in order to explain the blue scattering wings in the Lyα profiles seen in some of the observed positions.

P.G. thank the Centre National d'Etudes Spatiales (CNES), the University Pierre and Marie Curie, and the "Programme National de Cosmologie and Galaxies" (PNCG) and the "Physique Chimie du Milieu Interstellaire" (PCMI) programs of CNRS/INSU for their financial supports. We thank Daniel Kunth and Brigitte Rocca for very useful physical and technical discussions about Lyα scattering. Support for Program number HST-GO-13321.001-A was provided by NASA through a grant from the Space Telescope Science Institute, which is operated by the Association of Universities for Research in Astronomy, Incorporated, under NASA contract NAS5-26555. PA thanks Guillermo Blanc (Carnegie Observatories) and Emily Freeland (formerly Texas A&M University) for providing assistance with observations, and software/data reduction associated with the Mitchell Spectrograph. This work used observations carried out under project number U020 (P.I. Guillard) with the IRAM NOEMA Interferometer, reduced and analyzed with the GILDAS software (https://www.iram.fr/IRAMFR/GILDAS). IRAM is supported by INSU/CNRS (France), MPG (Germany) and IGN (Spain). We also thank the

referee who has contributed to improve both the figures and content of the paper.

ORCID iDs

P. Guillard https://orcid.org/0000-0002-2421-1350
P. N Appleton https://orcid.org/0000-0002-7607-8766
M. D. Lehnert https://orcid.org/0000-0003-1939-5885
M. E. Cluver https://orcid.org/0000-0002-9871-6490
C. K. Xu https://orcid.org/0000-0002-1588-6700
S. C. Gallagher https://orcid.org/0000-0001-6217-8101

References

Adams, J. J., Blanc, G. A., Hill, G. J., et al. 2011, ApJS, 192, 5
Alarie, A., & Morisset, C. 2019, RMxAA, 55, 377
Allen, M. G., Groves, B. A., Dopita, M. A., Sutherland, R. S., & Kewley, L. J. 2008, ApJS, 178, 20
Allen, R. J., & Hartsuiker, J. W. 1972, Natur, 239, 324
Appleton, P. N., Guillard, P., Boulanger, F., et al. 2013, ApJ, 777, 66
Appleton, P. N., Guillard, P., Togi, A., et al. 2017, ApJ, 836, 76
Appleton, P. N., Xu, K. C., Reach, W., et al. 2006, ApJL, 639, L51
Arp, H. 1973, ApJ, 183, 411
Blanc, G. A. 2013, AdAst, 2013, 641612
Cantalupo, S., Pezzulli, G., Lilly, S. J., et al. 2019, MNRAS, 483, 5188
Charlot, S., & Fall, S. M. 1993, ApJ, 415, 580
Cluver, M. E., Appleton, P. N., Boulanger, F., et al. 2010, ApJ, 710, 248
Decarli, R., Arrigoni-Battaia, F., Hennawi, J. F., et al. 2021, A&A, 645, L3
Dopita, M. A., & Sutherland, R. S. 1996, ApJS, 102, 161
Duarte Puertas, S., Iglesias-Páramo, J., Vilchez, J. M., et al. 2019, A&A, 629, A102
Duc, P.-A., Cuillandre, J.-C., & Renaud, F. 2018, MNRAS, 475, L40
Emonts, B. H. C., Cai, Z., Prochaska, J. X., Li, Q., & Lehnert, M. D. 2019, ApJ, 887, 86
Emonts, B. H. C., Lehnert, M. D., Dannerbauer, H., et al. 2018, MNRAS, 477, L60
Emonts, B. H. C., Lehnert, M. D., Villar-Martín, M., et al. 2016, Sci, 354, 1128
Falkendal, T., Lehnert, M. D., Vernet, J., De Breuck, C., & Wang, W. 2021, A&A, 645, A120
Fedotov, K., Gallagher, S. C., Konstantopoulos, I. S., et al. 2011, AJ, 142, 42
Fox, A. J., Ledoux, C., Petitjean, P., Srianand, R., & Guimarães, R. 2011, A&A, 534, A82
Gallagher, S. C., Charlton, J. C., Hunsberger, S. D., Zaritsky, D., & Whitmore, B. C. 2001, AJ, 122, 163
Ginolfi, M., Maiolino, R., Carniani, S., et al. 2018, MNRAS, 476, 2421
Green, J. C., Froning, C. S., Osterman, S., et al. 2012, ApJ, 744, 60
Gronke, M., Dijkstra, M., McCourt, M., & Oh, S. P. 2016, ApJL, 833, L26
Gronke, M., Dijkstra, M., Mccourt, M., & Peng Oh, S. 2017, A&A, 607, 71
Guillard, P., Boulanger, F., Cluver, M. E., et al. 2010, A&A, 518, A59
Guillard, P., Boulanger, F., Pineau Des Forêts, G., & Appleton, P. N. 2009, A&A, 502, 515
Guillard, P., Boulanger, F., Pineau Des Forêts, G., et al. 2012, ApJ, 749, 158
Hansen, M., & Peng, Oh, S. 2006, MNRAS, 367, 979
Heckman, T. M., Borthakur, S., Overzier, R., et al. 2011, ApJ, 730, 5
Hill, G. J., MacQueen, P. J., Smith, M. P., et al. 2008, Proc. SPIE, 7014, 701470
Hwang, J. S., Struck, C., Renaud, F., & Appleton, P. N. 2012, MNRAS, 419, 1780
Iglesias-Páramo, J., Lo´pez-Martín, L., Vílchez, J. M., Petropoulou, V., & Sulentic, J. W. 2012, A&A, 539, A127
Ji, S., Oh, S. P., & Masterson, P. 2019, MNRAS, 487, 737
Joshi, B. A., Appleton, P. N., Blanc, G. A., et al. 2019, ApJ, 878, 161
Konstantopoulos, I. S., Appleton, P. N., Guillard, P., et al. 2014, ApJ, 784, 1
Kwak, K., & Shelton, R. L. 2010, ApJ, 719, 523
Leclercq, F., Bacon, R., Wisotzki, L., et al. 2017, A&A, 608, A8
Lehmann, A., Godard, B., Pineau Des Forêts, G., & Falgarone, E. 2020, A&A, 643, A101
Leibler, C. N., Cantalupo, S., Holden, B. P., & Madau, P. 2018, MNRAS, 480, 2094
Marino, R. A., Cantalupo, S., Pezzulli, G., et al. 2019, ApJ, 880, 47
Moles, M., Sulentic, J. W., & Márquez, I. 1997, ApJL, 485, L69
Natale, G., Tuffs, R. J., Xu, C. K., et al. 2010, ApJ, 725, 955
Neufeld, D. A. 1990, ApJ, 350, 216
Neufeld, D. A. 1991, ApJL, 370, L85
Osterman, S., Green, J., Froning, C., et al. 2011, Ap&SS, 335, 257
O'Sullivan, D. B., Martin, C., Matuszewski, M., et al. 2020, ApJ, 894, 3
O'Sullivan, E., Giacintucci, S., Vrtilek, J. M., Raychaudhury, S., & David, L. P. 2009, ApJ, 701, 1560
Raga, A. C., Castellanos-Ramírez, A., Esquivel, A., Rodríguez-González, A., & Velázquez, P. F. 2015, RMxAA, 51, 229
Renaud, F., Appleton, P. N., & Xu, C. K. 2010, ApJ, 724, 80
Rodríguez-Baras, M., Rosales-Ortega, F. F., Díaz, A. I., Sánchez, S. F., & Pasquali, A. 2014, MNRAS, 442, 495
Shimakawa, R., Koyama, Y., Röttgering, H. J. A., et al. 2018, MNRAS, 481, 5630
Shull, J. M., & McKee, C. F. 1979, ApJ, 227, 131
Shull, J. M., & Slavin, J. D. 1994, ApJ, 427, 784
Slavin, J. D., Shull, J. M., & Begelman, M. C. 1993, ApJ, 407, 83
Sulentic, J. W., Rosado, M., Dultzin-Hacyan, D., et al. 2001, AJ, 122, 2993
Sutherland, R. S., & Dopita, M. A. 2017, ApJS, 229, 34
Tapken, C., Appenzeller, I., Noll, S., et al. 2007, A&A, 467, 63
Verhamme, A., Orlitová, I., Schaerer, D., & Hayes, M. 2015, A&A, 578, 1
Vernet, J., Lehnert, M. D., De Breuck, C., et al. 2017, A&A, 602, L6
Vidal-García, A., Falgarone, E., Arrigoni Battaia, F., et al. 2021, MNRAS, 506, 2551
Xu, C. K., Iglesias-Páramo, J., Burgarella, D., et al. 2005, ApJL, 619, L95
Xu, C. K., Lu, N., Condon, J. J., Dopita, M., & Tuffs, R. J. 2003, ApJ, 595, 665
Zheng, Z., & Miralda-Escude, J. 2002, ApJ, 578, 33